IEEE Access
Multidisciplinary | Rapid Review | Open Access Journal

Received 22 November 2023, accepted 6 December 2023, date of publication 18 December 2023,
date of current version 21 December 2023.

Digital Object Identifier 10.1109/ACCESS.2023.3343910

RESEARCH ARTICLE

Synthetic SAR Data Generator Using Pix2pix cGAN Architecture for Automatic Target Recognition

GUSTAVO F. ARAUJO[1], RENATO MACHADO[1], (Senior Member, IEEE), AND MATS I. PETTERSSON[2], (Senior Member, IEEE)

[1]Aeronautics Institute of Technology (ITA), São José dos Campos 12228-900, Brazil
[2]Blekinge Institute of Technology (BTH), 371 79 Karlskrona, Sweden

Corresponding author: Gustavo F. Araujo (gustavo.farhat@gmail.com)

This work was supported in part by the Brazilian Air Force; in part by the Brazilian Agencies National Council for Scientific and Technological Development (CNPq); in part by the Ministry of Science, Technology and Innovation (MCTI); in part by the Swedish-Brazilian Research and Innovation Centre (CISB), Saab AB; in part by the Coordination for the Improvement of Higher Education Personnel (CAPES) under Finance Code 001 (Pro-Defesa IV); and in part by the São Paulo Research Foundation (FAPESP) under Grant 2020/09838-0 (BI0S-Brazilian Institute of Data Science).

ABSTRACT Synthetic Aperture Radar (SAR) technology has unique advantages but faces challenges in obtaining enough data for noncooperative target classes. We propose a method to generate synthetic SAR data using a modified pix2pix Conditional Generative Adversarial Networks (cGAN) architecture. The cGAN is trained to create synthetic SAR images with specific azimuth and elevation angles, demonstrating its capability to closely mimic authentic SAR imagery through convergence and collapsing analyses. The study uses a model-based algorithm to assess the practicality of the generated synthetic data for Automatic Target Recognition (ATR). The results reveal that the classification accuracy achieved with synthetic data is comparable to that attained with original data, highlighting the effectiveness of the proposed method in mitigating the limitations imposed by noncooperative SAR data scarcity for ATR. This innovative approach offers a promising solution to craft customized synthetic SAR data, ultimately enhancing ATR performance in remote sensing.

INDEX TERMS Automatic target recognition, classification, conditional generative adversarial networks, data augmentation, Pix2Pix, synthetic aperture radar, synthetic data.

I. INTRODUCTION

Synthetic Aperture Radar (SAR) is a remote sensing technology used for decades in civil and military applications. SAR systems employ onboard radars on aircraft and satellites, transmitting pulses towards the ground. The backscattered signals, once received by the radar, are processed to produce representative images of the ground and targets located in the illuminated area [1]. SAR technology presents some particular capabilities compared to other technologies, such as optical and thermal imaging systems, producing high-resolution terrain images, regardless of whether clouds cover the illuminated region. It can also operate at night, as it is an active sensor and, therefore, does not need sunlight to illuminate the targets. Another important feature of SAR is its ability to differentiate target materials. The dielectric coefficient of each material plays an important role in attenuating more or less the backscattered signal [2].

A. AUTOMATIC TARGET RECOGNITION

Due to its particular capabilities, SAR is widely used in Automatic Target Recognition (ATR) applications. ATR is used to solve a series of everyday problems in which automatisms are created to recognize patterns in images and associate them with classes of interest. Among the main applications, we can highlight search and rescue services,

The associate editor coordinating the review of this manuscript and approving it for publication was Gerardo Di Martino.

traffic control, vessel monitoring, environmental policing, catastrophes monitoring, autonomous vehicles navigation, area security, and military operations [3].

ATR is subdivided into three sequential steps: detection, discrimination, and classification. In the detection, the main objective is to figure out the target candidates. Then, the discrimination algorithms evaluate the target candidates, rejecting those that do not fit to the sought pattern. Finally, after going through a training phase, the classification algorithms assign a label to each candidate target, associating it with a class [4].

B. CLASSIFICATION OF NONCOOPERATIVE TARGETS

Target classification algorithms must first be submitted to a very careful learning process to present reliable results. In such a learning process, whatever the approach is, there must be a variety of target samples relative to different poses that the target may appear in the image for each class of interest. We can find some SAR image datasets addressing ATR applications containing samples of targets [5], [6], where controlled campaigns were made with SAR systems mounted on aerial platforms, varying the azimuth or elevation angles relative to the target by one degree.

However, in the real world, target classes of interest are rarely cooperative and, therefore, not available for conducting a controlled experiment. In addition, some noncooperative targets are seldom exposed, making the image acquisition of those targets impracticable for training the classification algorithms. One possible approach is to use Electromagnetic Computing (EMC) software to produce synthetic data. Using a Three-dimensional Computer-Aided Design (3D-CAD) representative of the class of interest, the software simulates the transmission and reception of the radar signal, varying the angle of incidence relative to the target. With the synthetic raw data, a SAR image processing algorithm can be applied to generate a simulated SAR image.

It should be noted that even EMC software that uses asymptotic electromagnetic scattering prediction codes is characterized by a high runtime cost. They demand a long processing time and require memory and processing resources, sometimes making the application impractical.

C. PROPOSED METHOD FOR SYNTHETIC SAR DATA GENERATION

This paper proposes an alternative method for generating synthetic data of noncooperative targets with specific elevation and azimuth angles. A self-imposed constraint concerns the uncooperative characteristic of the considered targets. In such a case, measured data do not qualify as training inputs, so only synthetic data is used as input. Note that the proposed method is intended to be something other than self-sufficient in synthetic data generation since it uses synthetic data seeds as input.

The proposed approach aims to generate tailored synthetic data to alleviate the workload of the EMC software and to fill datasets with adequate missing data. The proposed method uses Conditional Generative Adversarial Networks (cGAN) to generate tailored synthetic data. Training with the synthetic data previously generated by the EMC software, the cGAN assimilates how small variations of the incidence angles impact the resulting SAR image. According to the pattern used during training, appropriate synthetic EMC data are presented as input to the cGAN, generating synthetic data whose targets are presented with parameterized elevation and azimuth angles.

Preliminary results, which suggested the possibility of applying the proposed method to ATR, can be found in [7].

D. OUTLINE

Section II presents the theoretical background of SAR and some applications in SAR ATR with GAN/cGAN. Section III introduces the methodology, presenting the original pix2pix cGAN and the modifications made in the algorithm for generating SAR synthetic data. The experiments carried out in this work are presented in Section IV, where we present the SAR model-based classification algorithm and the dataset used as a reference, the synthetic data generation process, and the analysis of the results. Finally, Section V presents the conclusions and final remarks.

II. GAN AND CGAN APPLICATIONS IN SAR ATR

To understand the growing importance of using cGANs in SAR ATR, we present some technologies that preceded it in the context of Artificial Intelligence (AI).

A. THEORETICAL BACKGROUND

Frank Rosenblatt, of the Cornell Aeronautical Laboratory at Cornell University, devised the Perceptron in 1957 under the sponsorship of the United States Naval Research, aiming to create a computer that could learn by trial and error, just as a human does [8]. The Perceptron was conceived as a simplified mathematical version of a brain neuron. It takes values as inputs, weights them, sums all the weighted values, and activates when the sum exceeds a threshold. The limitation of the Perceptron, given its single neuron architecture, led to the development of Neural Networks (NN): an arrangement of neurons where the output of one neuron is connected to the input of another. Using different activation functions, NN can capture nonlinear data characteristics and be used in regression and classification problems [9].

Regarding the image classification problem, Neural Networks, by directly connecting each pixel of an image to a neuron, present good results for classifying small images. However, the same performance cannot be obtained with larger images. To get around this problem, Cun et al. proposed the Convolutional Neural Networks (CNN) [10]. CNN can be used in images where objects appear in different sizes, perspectives, and positions. Unlike NN, which connects image pixels directly to neurons, CNN employs a series of

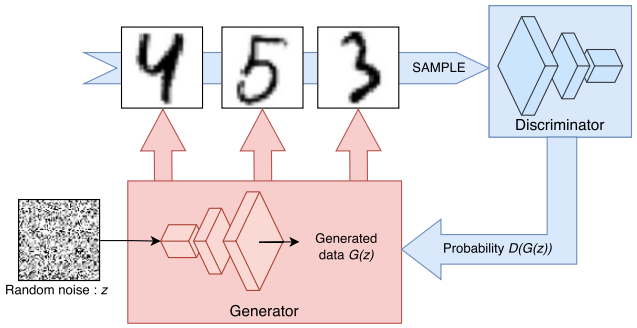

FIGURE 1. Example of a GAN generator training with MNIST dataset.

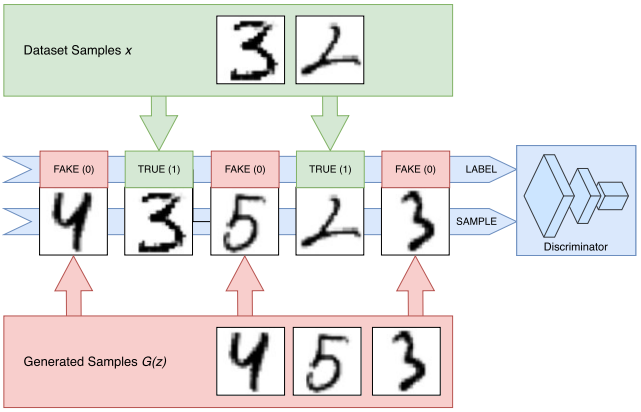

FIGURE 2. Example of a GAN discriminator training with MNIST dataset.

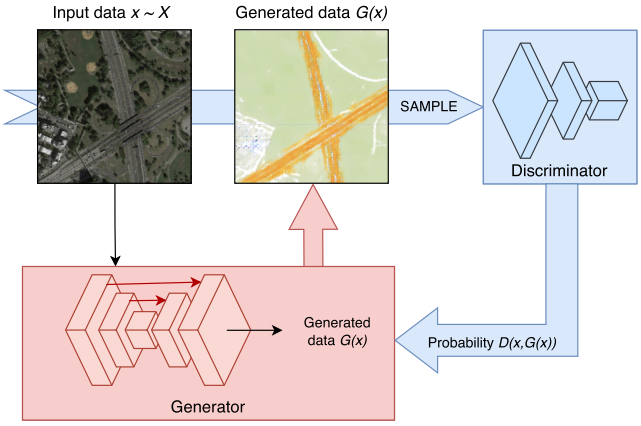

FIGURE 3. Example of a cGAN generator training applied for image translation.

image transformations, creating features connected to input neurons.

Goodfellow et al. proposed the first Generative Adversarial Networks (GAN) [11]. Inspired by the concept of game theory, they developed a CNN arrangement whose networks improve their performance by competing with each other. The two networks composing a GAN are the generator (G) and the discriminator (D). The generator aims to create samples that resemble those of the dataset so that it can deceive the discriminator, which, in turn, classifies samples as true or fake [11]. Performance optimization deals with two problems. The first one concerns the generator to minimize $\log(1 - D(G(z)))$. Starting from a random noise vector z, the generator learns to map an output image $G(z)$. $D(G(z))$ is the probability that $G(z)$ is derived from the dataset X. In Fig. 1, we can see an example used to generate digits according to the Modified National Institute of Standards and Technology (MNIST) dataset [12]. The generator training is carried out in cycles by sending its generated samples to the discriminator, which assigns the probability of each sample belonging to the dataset.

The optimization also deals with the maximization of $\log(D(x))$, which is the probability that samples x belonging to the dataset X are classified as such. As shown in Fig. 2, the discriminator is fed with samples originating from the dataset (x) and samples created by the generator ($G(z)$) so that each sample is labeled either one or zero, which means the probability of being true (dataset sample) or fake (generated sample), respectively. The discriminator then performs the learning process, improving it as the samples created by the generator also improve reliability. The objective function of this optimization process can be written as

$$V(G, D) = E_x[\log(D(x))] + E_z[\log(1 - D(G(z)))], \quad (1)$$

where E denotes the expectation operator, and the decision rule consists in $\arg\min_G \max_D V(G, D)$.

Conditional Generative Adversarial Networks (cGAN) are modified GAN arrangements that learn a mapping from observed data $x \sim X$ to another domain $y \sim Y$. The generator network (G), taking x as input, is trained to produce outputs $G(x)$ that cannot be distinguished from dataset data y by an adversary-trained discriminator network (D). Fig. 3 and 4 show respectively examples of cGAN generator and discriminator training applied to a problem for translating satellite images to map drawings [13].

The objective function of a cGAN can be expressed by

$$V(G, D) = \mathcal{L}_{\text{cGAN}}(G, D), \quad (2)$$

where the Loss Function is given by

$$\mathcal{L}_{\text{cGAN}}(G, D) = E_{x,y}[\log(D(x, y))] + E_x[\log(1 - D(x, G(x)))]. \quad (3)$$

The decision rule consists in $\arg\min_G \max_D V(G, D)$.

B. LITERATURE REVIEW

Since Goodfellow et al. introduced the first Generative Adversarial Networks (GAN), some works have addressed applications of those network types in SAR ATR [11]. Guo et al. were the first to implement an end-to-end GAN to simulate SAR images based on real images [14]. Lewis et al. investigated the use of GANs to make simulated data more realistic and, therefore, better suited to develop ATR algorithms for real-world scenarios [15]. They compared the use of two different GAN architectures to perform this task. In [16], Huang et al. presented a hierarchical

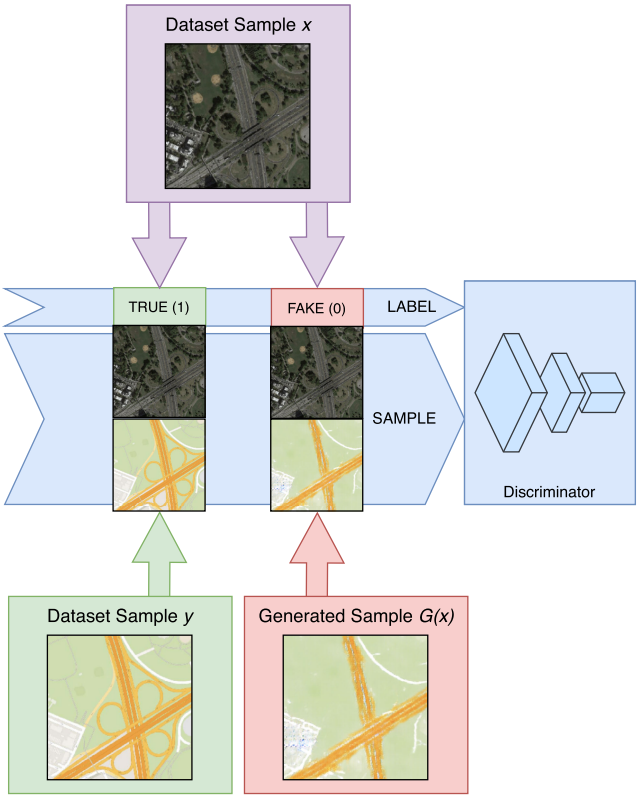

FIGURE 4. Example of a cGAN discriminator training applied for image translation.

GAN network model for generating high-resolution SAR images. In [17], Zhai et al. proposed a method to generate SAR image templates of targets from multiple angles. They used a Bayesian network to construct a GAN, in which the generative model and recognition model parameters are pre-trained with general datasets to obtain a GAN model that can generate SAR images from different azimuth angles. Zhang et al. proposed a semi-supervised transfer learning method based on GANs [18]. The discriminator of their GAN is redesigned with an encoder and a discriminative layer to make it capable of learning the feature representation of input data with unsupervised settings. In [19], Zheng et al. introduces a SAR ATR algorithm based on the combination of semi-supervised CNN and dynamic multi-discriminator GAN. In [20], Luo et al. proposed a method synthesizing minority class data by using Progressive Growing of GANs (PGGAN) for imbalanced SAR target recognition. Guo et al. presented a robust SAR ATR method via adversarial learning to integrate data denoising, feature extraction, and classification into a unified framework for joint learning [21]. Mao et al. developed a target recognition method of SAR image based on Constrained Naive Generative Adversarial Networks (CN-GAN) and Convolutional Neural Networks (CNN) [22]. In [23], Vint et al. designed a framework to perform SAR-based ATR in low-resolution Foliage Penetrating SAR images. They investigated the potential use of CNN and GANs to address the target recognition problem.

In [24], Hu et al. derived a deep generation as well as a recognition model based on Conditional Variational Auto-Encoder (CVAE) and GAN. A feature space for SAR-ATR was built based on the proposed CVAE-GAN model. Oh and Kim proposed a novel GAN-based multi-task learning (MTL) method for SAR target image generation, called PeaceGAN, that has two additional structures, a pose estimator and an auxiliary classifier, at the side of its discriminator to effectively combine the pose and class information via MTL [25]. Du and Zhang built a UNet-GAN to refine the generation of the SAR-ATR model adversarial examples. The UNet learns the separable features of the targets and generates the adversarial examples of SAR images [26]. In [27], Du et al. proposed a multi-constraint GAN (MCGAN) model, which can provide high-quality normalized images as the supplementary training dataset. They used an encoder to learn the features of the real images to enhance the similarity. Then, the encoded features were mixed with noise and category labels as the input of the generator to improve the diversity and category correctness. In [28], Ma et al. introduced an Open Set Recognition (OSR) method based on multi-task learning, developed from GAN, to overcome the problem of a classifier encountering targets from unseen categories and classifying them incorrectly. In [29], Du et al. proposed an Adversarial Encoding Network (AEN) that extracts physical-related features from simulated images for data augmentation through the adversarial learning of the encoder and the discriminator. Isola et al. investigated conditional generative adversarial networks (cGAN) as a general-purpose solution to image-to-image translation problems, proposing the pix2pix cGAN [13]. In [30], Grohnfeldt et al. presented the first cGAN architecture that was specifically designed to fuse Sentinel's SAR and optical multi-spectral (MS) image data to generate cloud- and haze-free MS optical data from a cloud-corrupted MS input and an auxiliary SAR image. In [31], He and Yokoya also simulated Sentinel's optical image from SAR data using cGAN. In [32], Bittner et al. introduced a new approach to generate an artificial Digital Surface Model (DSM) with accurate and realistic building geometries from City Geography Markup Language (CityGML) data by training a proposed cGAN architecture. Niu et al. adopted a cGAN to transform the heterogeneous SAR and optical images into some space where their information has a more consistent representation, making the direct comparison feasible [33]. When dealing with change detection, heterogeneous images are much more challenging than homogeneous images. In [34], Li et al. used a pix2pix network derived from cGAN to translate ISAR images to the corresponding optical images. They combined the generated and the original ISAR images to train a CNN network for recognition. Patel et al. put forward a novel concept of Polarimetric SAR (PolSAR) band-to-band image translation to synthesize multi-frequency PolSAR images from a single frequency PolSAR image [35]. They leveraged a Deep Neural Network (DNN), particularly a cGAN to perform the task. In [36], Ma et al. presented a weakly supervised algorithm

to perform the segmentation task for high-resolution SAR images. Their algorithm combines hierarchical cGAN and conditional random fields (CRF). Bermudez et al. proposed a new deep-learning-based framework to synthesize missing or corrupted multi-spectral optical images using multi-modal/multi-temporal data [37]. Specifically, they used cGAN to generate the missing optical image by exploiting the correspondent SAR data with SAR-optical data from the same area at a different acquisition date. In [38], Daquan et al. presented a Foliage Penetration (FOPEN) target detection method based on bi-frequency SAR and cGAN. They translate a high-frequency SAR image into a low-frequency one by means of a cGAN. In [39], Li et al. improved the interpretation of SAR images with a method of SAR-to-optical image translation, implementing a modified cGAN. Maggiolo et al. addressed the problem of automatic registration of multi-sensor images due to the inherently different physical, statistical, and textural properties of the input data [40]. For the case of Sentinel's optical and SAR images, they proposed a novel method based on a cGAN. Bjork et al. studied the generation of LiDAR-predicted above-ground biomass maps from SAR intensity images using cGAN [41]. In [42], Huang et al. proposed a novel fusion dehazing method to directly restore haze-free images by using an end-to-end cGAN. The proposed network combines the information of both optical and SAR images to eliminate image blurring. In [43], Wang et al. used cGAN to improve the Tomographic SAR (TomoSAR) reconstruction with a limited number of available SAR images. Turnes et al. proposed a novel cGAN architecture to improve the SAR-to-optical image translation [44]. The proposed generator and discriminator networks rely on atrous convolutions and incorporate an Atrous Spatial Pyramid Pooling (ASPP) module to enhance fine details in the generated optical image by exploiting spatial context at multiple scales. In [45], Christovam et al. proposed the addition of a Multi-Layer Perceptron loss function to the pix2pix cGAN objective function tackling the cloud-removal problem. In [46], Yang et al. proposed an improved cGAN (ICGAN) method for SAR-to-optical image translation. Finally, Wang et al. proposed a cGAN to generate targets with an intermediate azimuth. They used measured data as input and fake data for data augmentation with a feature-based classification algorithm [47].

III. METHODOLOGY

This paper proposes a methodology to generate new synthetic data based on the following target parameters: class, elevation angle, and azimuth angle. We disregard the use of measured data and EMC. Only previously obtained synthetic data, whether produced by EMC or not, can be used to generate new synthetic data.

A. PIX2PIX CGAN

The proposed methodology is based on the pix2pix cGAN [13]. The pix2pix cGAN is intended to be a general-purpose solution to image-to-image translation problems. They verified the success of applying this network in translating images between different domains. For example, experiments presented in [13] demonstrated the ability of pix2pix to translate street object labels to street scenes, building parts labels to facades, black and white images to color images, daytime landscape images to night images, caricatures to photos, thermal images to RGB photos and remote sensing optical images to cartographic maps.

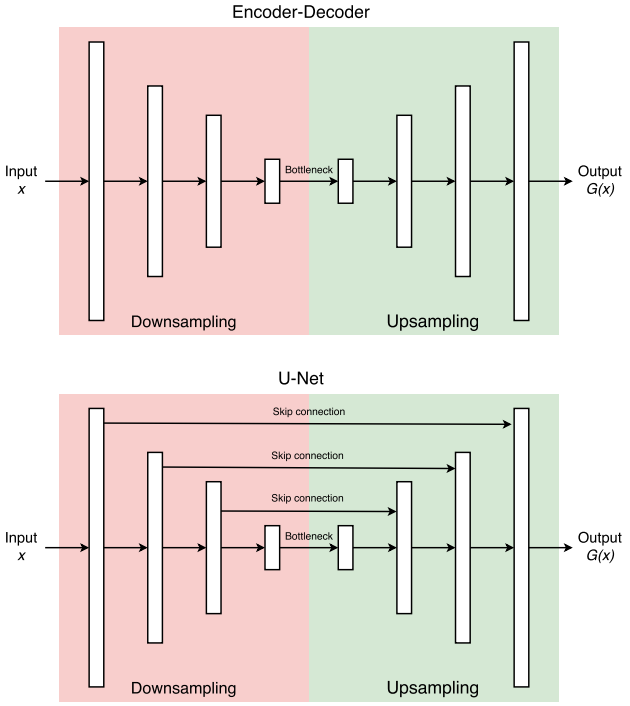

FIGURE 5. U-Net resulting from adding skip connections to the Encoder-Decoder network.

Their generator architecture uses an Encoder-Decoder network [48] as a starting point, in which an input image traverses layers down-sampling data to a bottleneck where the process is reversed to generate the output image. The bottleneck limits the amount of information passed from input to output. To work around this problem, the encoder-decoder architecture was modified to a typical U-Net architecture [49], which includes skip connections: connections between the mirrored input and output layers, i.e., the layers of the same dimension, as shown in Fig. 5.

They designed a discriminator architecture focused on local image patches called PatchGAN to model high-frequencies. The architecture of their discriminator also included an L1 term to force low-frequency correctness into the Loss Function. The discriminator classifies each patch as true or fake, averaging the entire image in a convolution way.

By adding the L1 distance, computed between the ground truth (y) and generated ($G(x)$) images,

$$\mathcal{L}_{\mathrm{L1}}(G) = E_{\mathrm{x,y}}[||y - G(x)||_1] \tag{4}$$

to the Loss Function (2), results the objective function of the pix2pix cGAN

$$V(G, D) = \mathcal{L}_{\text{cGAN}}(G, D) + \mathcal{L}_{\text{L1}}(G), \tag{5}$$

and the decision rule consists in $\arg\min_G \max_D V(G, D)$.

B. SAR SYNTHETIC DATA GENERATION WITH PIX2PIX CGAN

The proposed method aims to generate SAR synthetic data for target classes with different aspect angles (azimuth and elevation angles) using a modified pix2pix cGAN to perform interpolations and extrapolations. A simple linear interpolation could not be applied to SAR data since the backscattered signal does not vary linearly as the pose of the target changes.

Datasets prepared for ATR are comprised of chips (image clippings) of size $H \times V$ pixels, containing a single target in each chip. Those targets within the chips belong to any class (k) and appear in different aspect angles about the radar: azimuth (ϕ) and elevation (ω) or depression ($\theta = 90° - \omega$). The set of N classes $K = \{k \mid k \in \mathbb{Z}_+, k < N\}$ depends on the targets of interest and the application of the dataset. The sets of poses in which the targets can appear in relation to the azimuth angle (Φ) and to the depression angle (Θ) are obtained by defining

$$\Phi = \{\phi \mid \phi_{\text{i}} \leq \phi = \phi_{\text{i}} + n\Delta_\phi \leq \phi_{\text{f}}, n \in \mathbb{Z}_+, \Delta_\phi \in \mathbb{R}_+\} \tag{6}$$

and

$$\Theta = \{\theta \mid \theta_{\text{i}} \leq \theta = \theta_{\text{i}} + n\Delta_\theta \leq \theta_{\text{f}}, n \in \mathbb{Z}_+, \Delta_\theta \in \mathbb{R}_+\}, \tag{7}$$

where ϕ_{i} and ϕ_{f} set the range of the azimuth angle span, and Δ_ϕ is the angle increment step. The variables referring to the depression angle Θ are attributed in an analogous way to the azimuth angle Φ.

Using subsets of data chips whose class k and depression angle θ remain constant, whereas their azimuth angles ϕ vary with the same distances, we draw different interpolation/extrapolation patterns. Fig.6 illustrates twelve options of patterns using 3 (a-c), 4 (d-g), or 5 (h-l) chip subsets.

As an example, using xYx pattern (Fig. 6b), the modified pix2pix cGAN generator can be trained to carry out interpolations, generating SAR synthetic data chips Y_ϕ when the inputs are two chips containing targets of the same class k and depression angle θ but separated by two Δ_ϕ degrees in azimuth: $x_{\phi-\Delta_\phi}$ and $x_{\phi+\Delta_\phi}$. The Algorithm 1 describes this training process.

Fig. 7 illustrates how the generator is trained considering the pattern xYx, where two synthetic data chips, $x_{\phi-\Delta_\phi} = x(k, \theta, \phi - \Delta_\phi) = x(8, 17, 18)$ and $x_{\phi+\Delta_\phi} = x(k, \theta, \phi + \Delta_\phi) = x(8, 17, 20)$, are used as input. Note that their targets present the same class ($k = 8$) and the same depression angle ($\theta = 17°$), but their azimuth angles are spaced two degrees apart: $\phi - \Delta_\phi = 18°$ and $\phi + \Delta_\phi = 20°$ ($\Delta_\phi = 1°$). The generator outputs $G(x_{\phi-\Delta_\phi}, x_{\phi+\Delta_\phi})$, which is the prediction of $Y_\phi = Y(k, \theta, \phi)$, i.e., $Y(8, 17, 19)$. Y_ϕ is then sent along

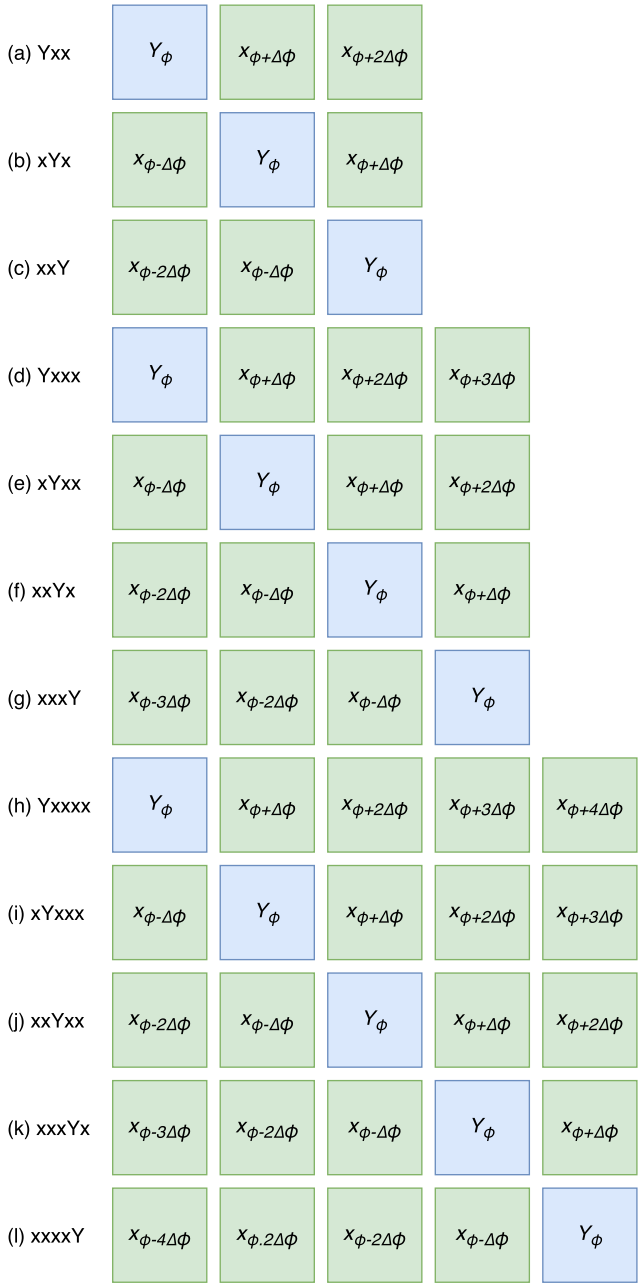

FIGURE 6. Examples of possible interpolation/extrapolation patterns.

to the discriminator with the generator input $x_{\phi-\Delta_\phi}$ and $x_{\phi+\Delta_\phi}$. The discriminator assigns a value between 0 and 1 to $D(x_{\phi-\Delta_\phi}, x_{\phi+\Delta_\phi}, Y_\phi)$, which means the probability that Y_ϕ is the corresponding interpolated image. The generator then uses this information to update its internal parameters with the goal of maximizing $D(x_{\phi-\Delta_\phi}, x_{\phi+\Delta_\phi}, Y_\phi)$. This whole process is repeated with different input pairs, varying class and aspect angles until a predetermined number of training epochs is reached.

In discriminator training, subsets labeled as "true" or "false" are presented to it. Both subsets contain the proper entries of the pattern in use (Fig. 6). What differs from the

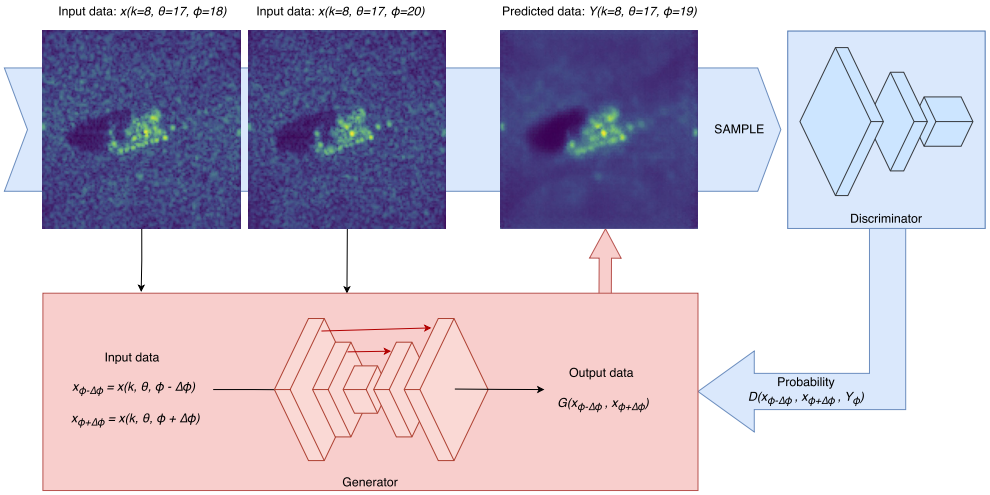

FIGURE 7. Example of pix2pix cGAN generator training by using *xYx* pattern.

Algorithm 1 Generator Training (pattern xYx)

Input: $x(k, \theta, \phi - \Delta_\phi)$,
$x(k, \theta, \phi + \Delta_\phi)$,
N ▷ Number of training epochs
Output: Y_ϕ
epoch $\leftarrow 1$
while epoch $\leq N$ **do**
$x_{\phi-\Delta_\phi} \leftarrow x(k, \theta, \phi - \Delta_\phi)$
$x_{\phi+\Delta_\phi} \leftarrow x(k, \theta, \phi + \Delta_\phi)$
$Y_\phi \leftarrow G(x_{\phi-\Delta_\phi}, x_{\phi+\Delta_\phi})$
Generator Updating $\leftarrow D(x_{\phi-\Delta_\phi}, x_{\phi+\Delta_\phi}, Y_\phi)$
epoch $\leftarrow$ epoch $+ 1$
end while

subsets is the translated image. In the case of the subset labeled as "true," the appropriate true data in the dataset are included. In the case of the subset labeled false, the data predicted by the generator are used.

In Fig. 8, we visualize an example of discriminator training considering the pattern xYx, where two labeled subsets are presented to the discriminator. Both subsets contain $x_{\phi-\Delta_\phi}$ and $x_{\phi+\Delta_\phi}$. However, whereas the subset labeled "true" includes x_ϕ, the subset labeled "false" includes Y_ϕ).

We highlight that the reason for choosing pix2pix cGAN relies on the fact that it works with paired images. It means the translated image (output) must be related to the source image (input). Other types of networks are also capable of translating images between different domains, but, working in an unpaired way, they could not capture the features related to each pair. For example, CycleGAN translates images between two different domains by learning from two domains and then translates images from one domain to another. This way, it could not work for our proposed application since, in our case, the supposed two domains are actually only one. Thus, there would be nothing to be learned by the CycleGAN,

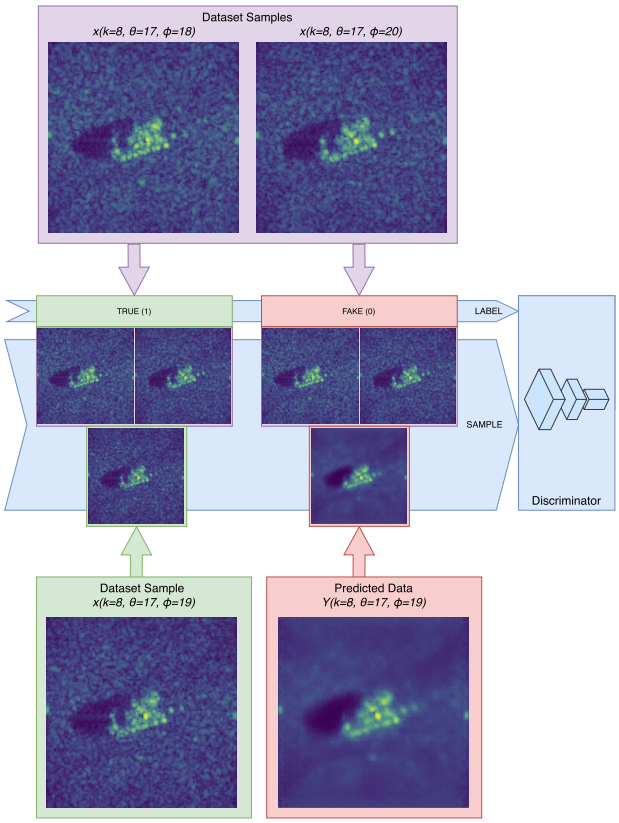

FIGURE 8. Example of pix2pix cGAN discriminator training by using *xYx* pattern.

as it would be demanded to translate from one domain to itself.

C. MODIFIED PIX2PIX CGAN

The originally designed pix2pix cGAN has some characteristics that require adaptations or modifications to meet the proposed methodology for generating SAR synthetic data.

1) INPUT CHANNELS

The original pix2pix cGAN takes RGB image chips as input, which means that the input image is made up of three channels. The modified pix2pix cGAN considers single-polarization SAR imaging chips as input, which are represented in a single channel. However, the number of input chips depends on the selected pattern (Fig.6). So, the pix2pix cGAN is changed by assigning each input chip to a new channel. Therefore, the number of input channels varies according to the selected pattern.

2) OUTPUT CHANNELS

Like the input image, the output image of the original pix2pix cGAN is also an RGB image, which has three channels. As the result of the interpolation/extrapolation is a single polarization SAR chip image, only one output channel is used, and the other two are ignored.

3) CHIP SIZE

The dimensions of the chips used by the original pix2pix cGAN are 256×256 pixels. The dataset chips (Section IV-B) used for the experiments have dimensions of 128×128 pixels. Therefore, the generator and discriminator architectures had to be changed to fit their dimensions. Thus, the first and last coding/decoding convolution stages of the generator U-Net network were excluded, as well as the first convolution stage of the discriminator.

IV. EXPERIMENTS AND RESULTS

In general, image generation algorithms aim to produce fake images as similar as possible to true images. However, a method to assess such similarity depends on the purpose and application of the images. In most cases, especially when the human eye is confronted with such a judgment, subjectivity is a dominant factor that makes an accurate assessment difficult. In this work, such difficulty does not exist since the generated images are intended to be used as a basis for target classification. Therefore, it is possible to compare the results of target classification using two different sets of data as a basis for classification: one containing only EMC synthetic data and the other containing only fake synthetic data whose targets have the same classes and aspect angles. In previous work, the authors proposed an algorithm for classifying noncooperative targets in SAR images [50]. The proposed algorithm presents a model-based approach using EMC synthetic data for creating models. Those models are then used for generating and verifying hypotheses, assigning classes and aspect angles to the target under classification [4].

A. SAR MODEL-BASED CLASSIFICATION ALGORITHM

The previously proposed SAR model-based classification algorithm [50] is based on EMC synthetic data chips, from which the N scattering centers of higher amplitude and their respective coordinates are extracted. A model is created for each combination of class and aspect angle available in the dataset by weighting the scattering centers of the extracted set. When a target (measured data) is submitted for classification, its aspect angles are estimated, and the same number of N strongest scattering centers is extracted. Then, considering the models whose aspect angles are within a tolerance regarding the estimated aspect angle, the hypotheses that a target may belong to each class of interest are constructed. Finally, through a Likelihood Ratio Test specially designed to match the positions of the scattering centers, the hypotheses are verified to determine the predicted class of the target. As small variations in the acquisition geometry substantially influence the resulting SAR image, the lack of some models can strongly impact the performance of the classification algorithm. As the previously proposed algorithm is model-based, it is highly dependent on the completeness of a dataset in relation to the existence of synthetic data for each target class and aspect angles since the reference models are created from those data.

B. SAMPLE DATASET

A partnership between the Wright State University and the Air Force Research Laboratory (AFRL) resulted in the elaboration of a dataset specially designed for automatic target recognition applications. The dataset called Synthetic and Measured Paired Labeled Experiment (SAMPLE) was made available to the academic and research communities in 2019 [6]. As an upgrade of the Moving and Stationary Target Acquisition and Recognition (MSTAR) dataset [5], which has been addressed for decades, the SAMPLE dataset results from meticulous work to produce reliable data. i The MSTAR dataset was obtained through a controlled experiment that used an airborne radar operating in the X band. The data set contains ten categories of military vehicle targets. The MSTAR dataset was used to generate the SAMPLE dataset, which has 1345 synthetic data chips (128×128 pixels), each containing a target (vehicle), matching classes and aspect angles to the MSTAR measured data chips.

The SAMPLE dataset contains targets of ten different classes (k) with depression angle (θ) varying between 14° and 17° in one-degree increments ($\Delta_\theta = 1°$) and azimuth angle (ϕ) ranging from 10° to 80° also with increment of one degree ($\Delta_\phi = 1°$). However, chips are missing for certain combinations of class and depression/azimuth angles. Fig. 9(a-d) details the content of the SAMPLE dataset by representing existing chips in green and the missing chips in red. Note that each diagram within the figure refers to a different depression angle θ. Their columns represent the azimuth angle ϕ, and their rows the target classes k.

C. CLASSIFICATION BASED ON EMC SYNTHETIC DATA

For each MSTAR measured data chip used by the SAMPLE dataset there is a synthetic data chip comprising a simulated target of the same class and aspect angles (depression and azimuth). The synthetic data in the SAMPLE dataset, produced using an Electromagnetic Computing (EMC) tool, are very reliable because the physical characteristics of the

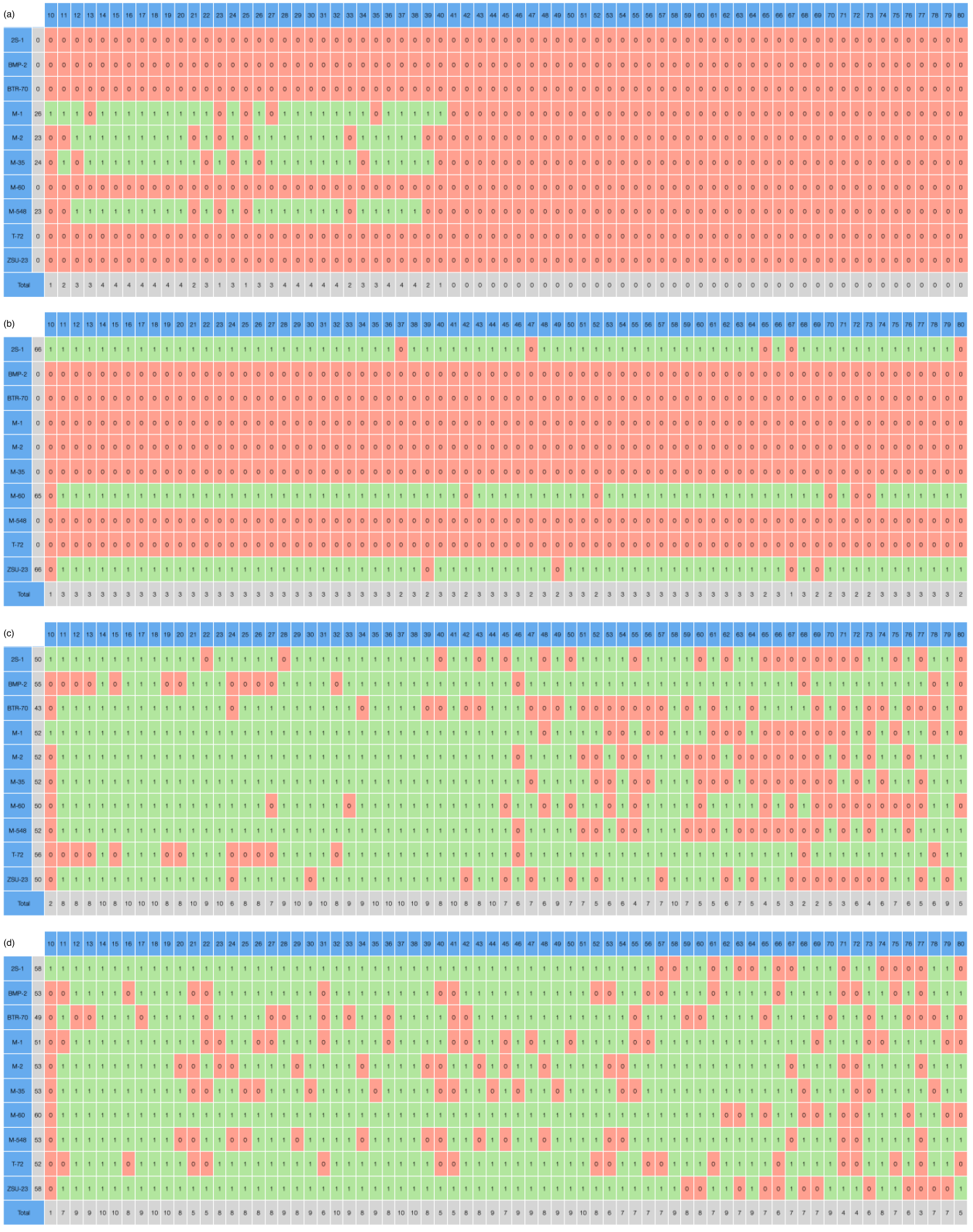

FIGURE 9. Existing chips (green) and missing chips (red) in the SAMPLE dataset for the depression angle (a) $\theta = 14°$, (b) $\theta = 15°$, (c) $\theta = 16°$, and (d) $\theta = 17°$.

TABLE 1. Pairs of aspect angles used in the experiments.

Depression Angle θ	Azimuth Angle ϕ
16°	14°, 16°, 17°, 18°, 21°, 23°, 29°, 31°, 35°, 36°, 37°, 38°, 41°, 44°, and 58°
17°	14°, 15°, 18°, 19°, 32°, 37°, 38°, and 51°

targets have been considered to have the smallest detail when introduced to the simulation. Characteristics of each target section, such as geometry, materials, and dielectric properties, were surveyed in the field and inserted into the configuration of CAD-3D models used by the EMC tool. Fig. 10 illustrates an example of measured and synthetic data within the SAMPLE dataset relative to all ten classes with the same depression and azimuth angles.

For the experiments with the model-based classification algorithm previously proposed by the authors [50], the EMC synthetic data contained in the SAMPLE dataset were used as the source to create the models and thus construct the hypotheses. The measured data from the MSTAR dataset were subjected to classification to assess the algorithm performance. Considering the incompleteness of the SAMPLE dataset, the authors used only those chips whose pairs of aspect angles exist for all ten classes of targets. The reason for that data restriction lies in the concern that all ten classes could be assigned to a target with equal probability. So, inspecting the SAMPLE dataset, they found 23 pairs of aspect angles that meet the requirement. Consequently, 230 chips were used in their experiments. The 23 pairs of aspect angles considered in the experiments are listed in Table 1.

Experiments with different configurations of the algorithm were performed. One of those configurations, the Modified Likelihood Ratio Test / Scattering Centers (MRLT/SC), reached a Percentage of Correct Classification (PCC) of 86.96%. Given its excellent performance and ease of application, we chose to use that configuration as a reference for comparing results in the current work.

The scope of the research demands no leaking between measured and simulated data, as it assumes a scenario where no measured data is available for training. This is the reason why we only use simulated EMC data for training. We do not intend to assess the classification algorithm using MSTAR data for training. The comparison in classification is done by using MSTAR-measured data as testing images and varying the basis for classification between EMC data and pix2pix generated data.

D. GENERATION OF FAKE SYNTHETIC DATA

Before generating fake synthetic data, it is necessary to prepare the EMC synthetic data of the SAMPLE dataset and define the interpolation/extrapolation patterns to be used for training the pix2pix cGAN. The SAMPLE dataset chips store the complex value of each scattering center. After we convert and assign the amplitude to each pixel, they can assume any real value greater than zero. Since the pix2pix cGAN is configured to handle pixel values between -1 and $+1$, each EMC synthetic data chip is normalized such that,

$$\tilde{x}(k,\theta,\phi) = 2\frac{x(k,\theta,\phi) - \min(x(k,\theta,\phi))}{\max(x(k,\theta,\phi)) - \min(x(k,\theta,\phi))} - 1. \quad (8)$$

According to Fig. 6, we select the patterns Yxx, xYx, and xxY to train the pix2pix cGAN. Inspecting the SAMPLE dataset, we found 907 subsets that fit each of those patterns. Then, the subsets whose "Y chip" aspect angles were used by the previously proposed algorithm, i.e., those listed in Table 1, were placed aside to be used for testing. The subsets separated for testing, according to each of the three patterns (Yxx, xYx, and xxY), were respectively 170, 180, and 186. Fig. 11 depicts by means of a diagram the distribution of chips used by the previously proposed classification algorithm, considering the possibility of generating them using each pattern. It means that out of the 230 chips used previously, 222 can be generated using the three patterns together.

After removing the subsets used for testing, 727, 737, and 721 subsets remain to be used in training patterns Yxx, xYx, and xxY, respectively. We perform a training effort comprising 200 epochs for the three patterns, Yxx, xYx, and xxY. A randomly selected number of subsets equal to the number of training subsets (737, 727, and 721) is used in each training epoch. At the end of each training epoch, 170, 180, and 186 fake synthetic data chips are generated for each pattern, Yxx, xYx, and xxY, respectively. In Fig. 12, we illustrate an example where a trained xYx pix2pix cGAN is used to generate fake synthetic data chips. We show both input chips, the ground truth, and output (predictions) after 1, 10, 100, and 200 training epochs.

By visually inspecting the images, we assessed the output images in different epochs. After the first training epoch, we observed that the output image presents the target with an aspect very close to the ground truth. However, the image presents a general blurring. After the tenth epoch, we can already observe an image with greater definition, even though the background still presents a lot of blurring. After the 100^{th} and 200^{th} epochs, we observed almost no difference between the output images, which in turn are already as sharp as the Ground Truth.

As stated at the beginning of this section, human eyes are not the most suitable tools to measure the similarity between the generated images and ground truth when dealing with ATR applications. So, we performed two different analyses: one to verify convergence along the training epochs in producing images similar to the ground truth and another to test the hypothesis that the generated fake synthetic data are more similar to the ground truth than their EMC synthetic data input. The last one is also valid to verify if the output image is subjected to bias by collapsing to one of its inputs.

1) CONVERGENCE ANALYSIS

For each training pattern (Yxx, xYx, and xxY) and at every training epoch, we used three metrics to assess the

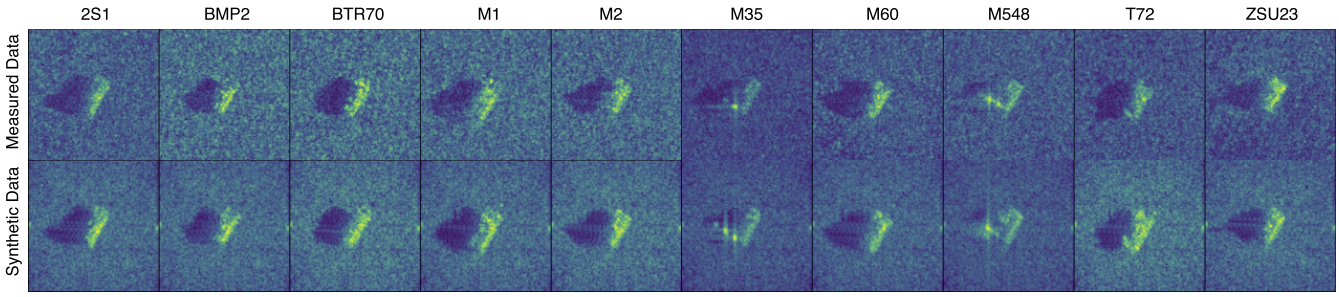

FIGURE 10. Example of measured and synthetic data chips regarding the ten classes found in the SAMPLE dataset.

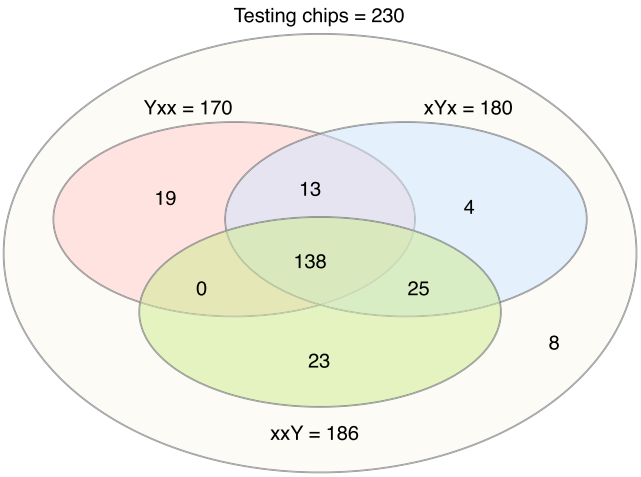

FIGURE 11. Number of fake chips generated using patterns Yxx, xYx, and xxY.

convergence of the generated image towards the ground truth. Between each of the predicted images (fake synthetic data) and the ground truth (EMC synthetic data), we calculated the Mean Squared Error (MSE), Pearson's Chi-Square statistic test, and the correlation with the Histogram Comparison. Figures 13, 14, and 15 plot the average MSE of 200 training epochs for Patterns Yxx, xYx, and xxY, respectively.

Figures 13, 14, and 15 also show the impact of the clutter by plotting its MSE. The targets were disregarded for this analysis. Therefore, all pixels whose Euclidean distances from the center of the chips are greater than 50 were sampled, considering only them as part of the background, i.e., clutter. As expected, the level of the backscattered signal on the clutter region is very low compared to the target region. Consequently, the average MSE of the clutter is also low and almost constant along the training epochs. Therefore, it shows that if the cGAN has difficulties in capturing background randomness, there will be no substantial impacts in minimizing the Loss Function, which will be more sensitive to the target region since the latter has a higher signal level.

Regardless of the pattern used, we noticed that, as the number of training epochs increases, the MSE rapidly converges until it reaches an optimal value in a range with small oscillations, somewhere between 75 and 200 training epochs.

The Pearson's Chi-Square test was also carried out to verify the similarity of data by considering each scattering center location a category. The Pearson's Chi-Square test is given by

$$\chi^2 = \sum_{i=1}^{N} \frac{(O_\mathrm{i} - E_\mathrm{i})^2}{E_\mathrm{i}}, \tag{9}$$

where O_i is the normalized amplitude of the i^{th} scattering center in the fake synthetic data (observed image) and E_i is the normalized amplitude of the scattering center at the same position, but in the ground truth (expected image).

Figures 16, 17, and 18 confirm the results obtained in the MSE test. As can be seen, the results of Pearson's Chi-Square test demonstrate that, even though clutter has great relevance in this statistical calculation, the differences between the generated fake image and the ground truth converge to minimum values as the number of training epochs increases.

Still to check the convergence of the images in relation to the ground truth, we performed a Histogram Comparison using the correlation coefficient as a metric. A Histogram Comparison expresses how well two histograms match with each other. Using the pixel amplitude data as a basis, the images generated at each training epoch were transformed into histograms, and the same was done with the ground truth. The average correlation coefficients found in each training epoch for each of the patterns used are plotted in Fig. 19.

We can verify that for all three patterns used (Yxx, xYx, and xxY) the correlation coefficient increases progressively, corroborating the other two tests (Mean Square Error and Pearson's Chi-Square) in the conclusion that the predicted images converge on the ground truth image.

Although this work considers a scenario in which the targets are uncooperative and their measured data is not available, we perform the same Histogram Comparison test, but now we replace the ground truth (Synthetic EMC data) with the MSTAR measured data. Fig. 20 shows as expected, smaller correlation coefficients since MSTAR data was not used as a basis for image prediction. However, as can be seen, in the three patterns used (Yxx, xYx, and xxY) the results continue to converge as training epochs progress.

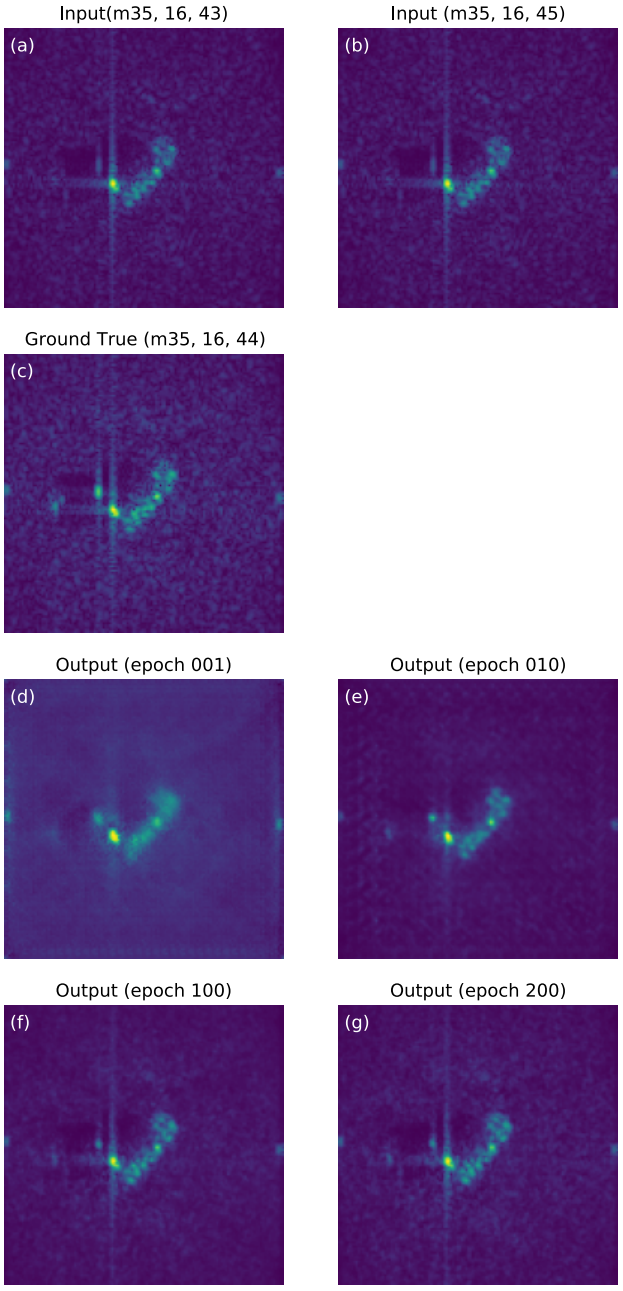

FIGURE 12. Example of fake synthetic data generation of a M35 class target at 16° depression angle and 44° azimuth angle. From left to right and from top to bottom: (a) and (b) two input EMC synthetic data chips according to xYx pattern, (c) ground truth and predictions, after (d) 1, (e) 10, (f) 100, and (g) 200 training epochs.

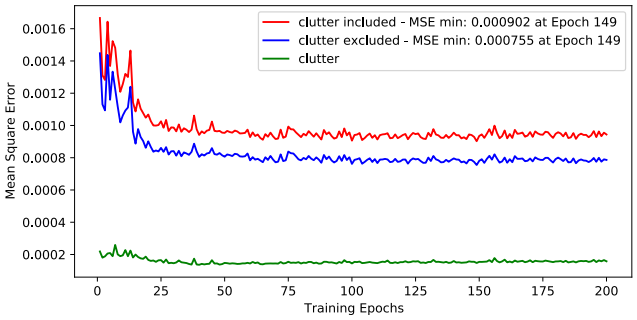

FIGURE 13. Average Mean Squared Error of 170 Yxx pix2pix cGAN predicted images at each training epoch. Clutter MSE was computed to investigate its impact on the chip MSE convergence.

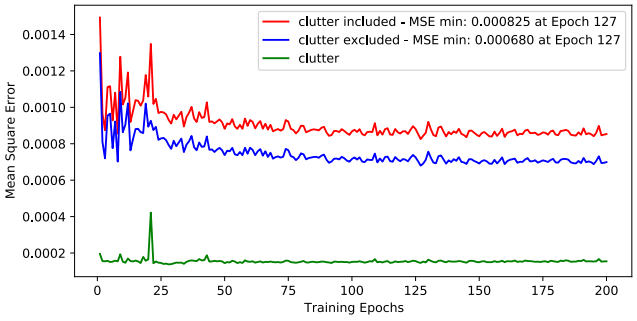

FIGURE 14. Average Mean Squared Error of the 180 xYx pix2pix cGAN predicted images at each training epoch. Clutter MSE was computed to investigate its impact on the chip MSE convergence.

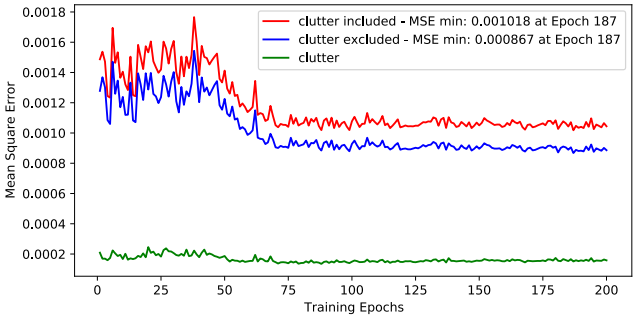

FIGURE 15. Average Mean Squared Error of the 186 xxY pix2pix cGAN predicted images at each training epoch. Clutter MSE was computed to investigate its impact on the chip MSE convergence.

2) COLLAPSING ANALYSIS

Some questions may arise regarding the pix2pix cGAN outputs, for example: Do the data generated by the pix2pix cGAN resemble ground truth more than the inputs used for its generation? Are the outputs just collapsing to one of their inputs? To answer those questions, we performed an analysis where, in addition to comparing the ground truth with the generated image, we also compared the ground truth with the two input images used to generate the output image by calculating their MSE.

Inspecting Fig. 21 and 22, which refer to the patterns Yxx and xYx respectively, taking the ground truth as references, we note that with more than 50 training epochs the pix2pix cGAN produces output images with lower MSE compared to the ones produced by the input images. For the xxY pattern, shown in Fig.23, the MSE is a little smaller than the one for the generated by fake synthetic data.

The consideration above can be confirmed by hypothesis tests. Considering a number of training epochs greater than 75, according to the graphs from that point on the results stabilize around an average. We assume that those results

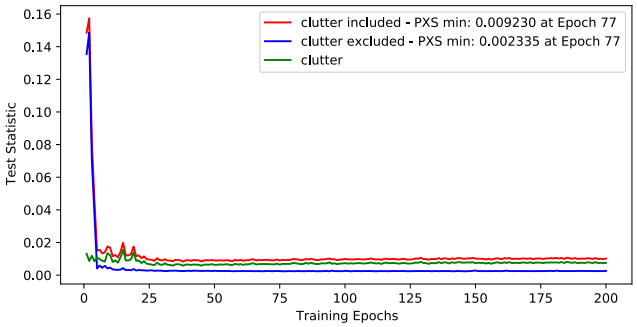

FIGURE 16. Average Pearson's Chi-Square test of the 170 Yxx pix2pix cGAN predicted images at each training epoch.

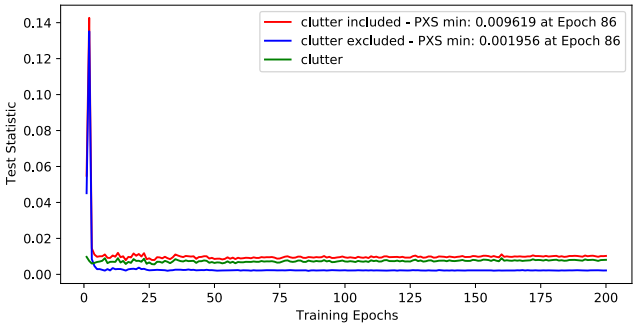

FIGURE 17. Average Pearson's Chi-Square test of the 180 xYx pix2pix cGAN predicted images at each training epoch.

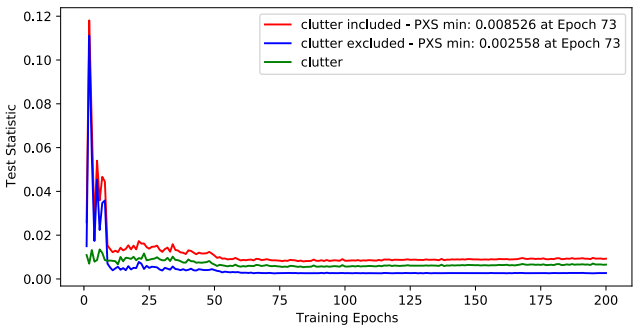

FIGURE 18. Average Pearson's Chi-Square test of the 186 xxY pix2pix cGAN predicted images at each training epoch.

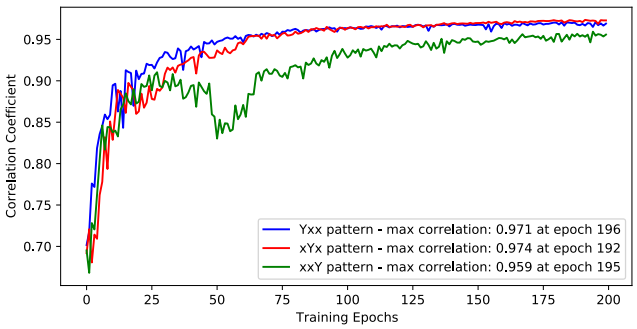

FIGURE 19. Average Histogram Comparison correlation coefficient between predicted images and ground truth at each training epoch.

follow a normal distribution. This way we can verify whether the fake synthetic data resemble Ground Truth more than those EMC synthetic data used as input do.

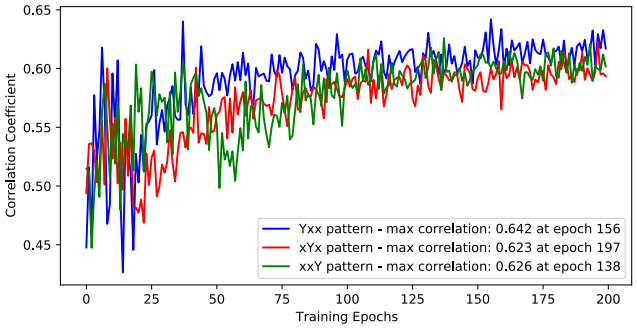

FIGURE 20. Average Histogram Comparison correlation coefficient between predicted images and MSTAR measured data at each training epoch.

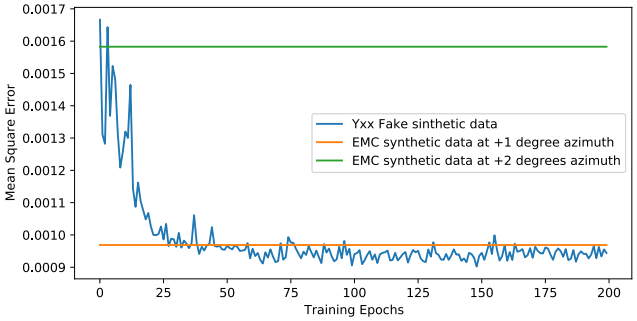

FIGURE 21. Average Mean Squared Error between Ground Truth and: Yxx pix2pix cGAN predicted images, input image at +1°, and input image at +2° azimuth angle.

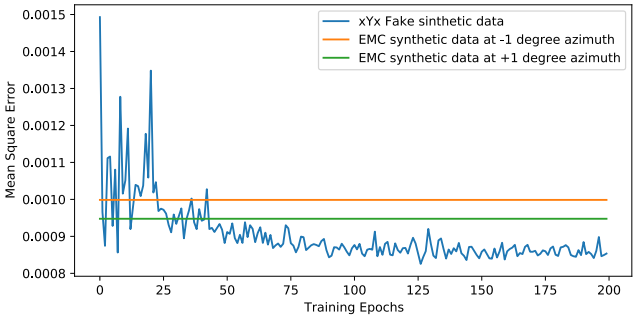

FIGURE 22. Average Mean Squared Error between ground truth and: xYx pix2pix cGAN predicted images, input image at −1°, and input image at +1° azimuth angle.

With a confidence level of 99% and using the t-distribution, for each of the patterns, within the range from the 76th to the 200th training epoch, we tested the hypotheses of the calculated MSE between the fake synthetic data and the Ground Truth being significantly smaller than the lowest MSE calculated between each of its EMC synthetic data inputs and the Ground Truth. Table 2 summarizes the tests.

As can be seen, the MSE hypotheses of the images generated using the patterns Yxx and xYx, significantly smaller than those of their inputs, are accepted. The same cannot be said about the xxY pattern, as this hypothesis is rejected.

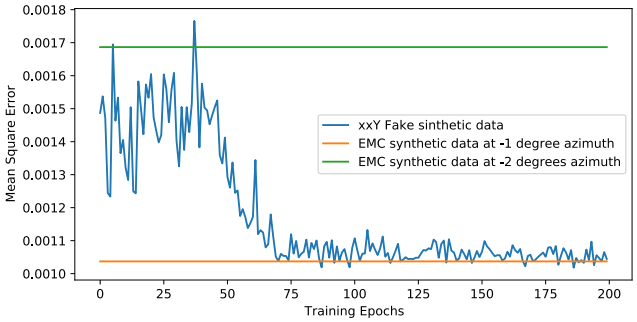

FIGURE 23. Average Mean Squared Error between ground truth and: xxY pix2pix cGAN predicted images, input image at −1°, and input image at −2° azimuth angle.

TABLE 2. MSE hypothesis tests.

Pattern	Yxx	xYx	xxY
$\min(\text{MSE}_{\text{input}}) \times 10^{-3}$	0.969	0.948	1.037
$\text{mean}(\text{MSE}_{\text{fake}}) \times 10^{-3}$	0.941	0.864	1.062
$\text{std dev}(\text{MSE}_{\text{fake}}) \times 10^{-3}$	0.017	0.016	0.023
$H_0 : \text{MSE}_{\text{fake}} \geq \text{MSE}_{\text{input}}$	rejected	rejected	accepted
$H_a : \text{MSE}_{\text{fake}} < \text{MSE}_{\text{input}}$	accepted	accepted	rejected
Degrees of freedom	124	124	124
$t_{\alpha=1\%}$	−2.3568	−2.3568	−2.3568
t_{obs}	−17.9737	−57.3224	12.3225

Answering the questions posed earlier, we can say, with a confidence level of 99%, that the fake synthetic data generated by Yxx and xYx pix2pix cGAN are significantly more similar to ground truth than the EMC synthetic data inputs. We can also conclude that the generated images do not collapse to any of their respective inputs.

E. CLASSIFICATION BASED ON FAKE SYNTHETIC DATA

The experiments carried out in Sections IV-D1 and IV-D2 are important to show that fake synthetic data have a better similarity to ground truth compared to any EMC synthetic data whose target presents small angular variations. However, those experiments are not sufficient to assess whether fake synthetic data can efficiently replace synthetic EMC data as the basis for a model-based target classification algorithm. A low MSE indicates only a similarity between the Fake synthetic data and the ground truth EMC synthetic data as a whole. There is no guarantee that the pixels produced by the most impactful scattering centers, which are extremely important in producing features for the classification algorithm, will keep the same relationship.

We designed experiments to verify the applicability of fake synthetic data as a basis for the previously proposed target classification algorithm. In the experiments, we tried to replace EMC synthetic data with fake synthetic data as much as possible. As shown in Fig. 11, eight out of the 230 chips used for testing do not have the required inputs so that the pix2pix cGAN could generate them. Therefore, a total of 222 fake synthetic data chips and eight original EMC synthetic data chips were used in the experiments.

TABLE 3. Test sets used in the classification experiment and the number of chips from each pattern compounding them.

Test Set	Priority 1	Priority 2	Priority 3	Priority 4
1	Yxx (170)	xYx (29)	xxY (23)	EMC (8)
2	Yxx (170)	xxY (48)	xYx (4)	EMC (8)
3	xYx (180)	Yxx (19)	xxY (23)	EMC (8)
4	xYx (180)	xxY (23)	Yxx (19)	EMC (8)
5	xxY (186)	xYx (17)	Yxx (19)	EMC (8)
6	xxY (186)	Yxx (32)	xYx (4)	EMC (8)

TABLE 4. Probability of Correct Classification (PCC) using the test sets as the basis for classification.

Test Set	Percentage of Correct Classification (PCC)			
	Fake Synthetic Data			Int./Ext.
	max	$75 < \text{epoch} \leq 200$		
		mean	std_dev	
1	0.8391	0.8097	0.0082	0.6261
2	0.8522	0.8140	0.0100	0.6478
3	0.8478	0.8218	0.0087	0.7087
4	0.8478	0.8218	0.0087	0.7087
5	0.8522	0.8209	0.0101	0.6043
6	0.8478	0.8217	0.0094	0.6348
Average	0.8399	0.8183	0.0058	0.6551

Considering the three sets of fake synthetic data generated with each training pattern of the pix2pix cGAN (Yxx, xYx and xxY), containing respectively 170, 180, and 186 overlapping chips, we created six test sets, each containing 222 chips of fake synthetic data. What differentiates the six test sets is the origin of the chips that comprise them. Each test set is populated following a different order of priority that combines the three patterns used to generate the data. Table 3 details the origin of the chips that comprise each test set.

One detail should be noted: We have only 5 test sets since test sets 3 and 4 are identical. The chips generated by both patterns Yxx and xxY, which do not exist in pattern xYx, do not intersect.

The same experiments performed with the previously proposed algorithm, which originally used SAMPLE dataset EMC synthetic data as a basis for measured data classification, were repeated this time using each test set as the basis. Table 4 summarizes the results obtained by detailing the maximum PCC found for each test set of fake synthetic data and the mean and standard deviation. In addition, it presents the average results of all tests in the last row.

Obviously, we could not expect the results to surpass the Percent of Correct Classification (PCC) of 86.96% achieved when using the original EMC synthetic data from the SAMPLE dataset. That PCC must be considered as a ceiling because if the fake synthetic data had been generated exactly the same as the synthetic EMC data, the same PCC would have been reached. It makes no logical sense for the fake synthetic data to be "more accurate" than the original EMC synthetic data. Observing the maximum PCC reached when using each of the test sets, we verify that the test sets with the best performance (test sets 2 and 5) reached a PCC of 85.22%, i.e., only 1.74% below the reference

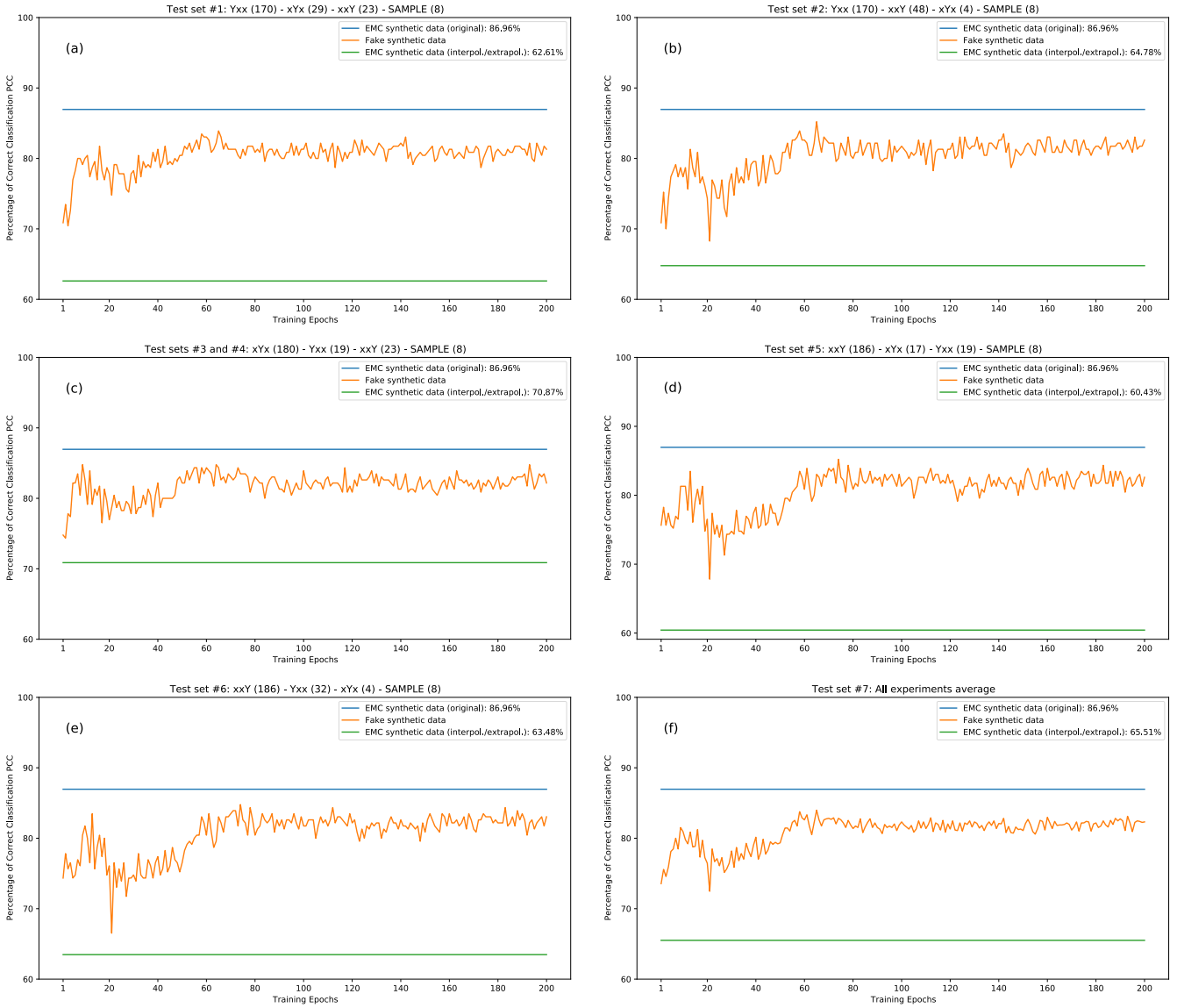

FIGURE 24. Comparison of classification results: (a) test set #1, (b) test set #2, (c) test sets #3 and #4, (d) test set #5, (e) test set #6, (f) test sets average.

value – 86.96% when using original EMC synthetic data. However, in the worst case (test set 1), a PCC of 83.91% was reached – 3.05% below the reference. Taking the average of the test sets, we verified a maximum PCC of 83.99%, representing 2.97% below the reference. Although we did not verify optimal results, they are very close to the reference values. Those results, presenting fake synthetic data as a good alternative in the absence of EMC synthetic data, indicate a real possibility that they could be used as a basis for the classification algorithm.

Finally, to answer a question that puzzled us during the research, we evaluated the hypothesis that the results obtained with the fake synthetic could not significantly surpass a simple arithmetic interpolation/extrapolation. We created one subset of data by interpolating the same input chips we used to generate the fake synthetic data on the xYx pattern.

By calculating

$$x_{\mathrm{xYx}}(k,\theta,\phi) = \frac{x(k,\theta,\phi-\Delta_\phi) + x(k,\theta,\phi+\Delta_\phi)}{2}, \quad (10)$$

we obtained 180 xYx pattern interpolated chips. By applying

$$\begin{aligned} x_{\mathrm{Yxx}}(k,\theta,\phi) &= 2\,x(k,\theta,\phi+\Delta_\phi) - x(k,\theta,\phi+2\Delta_\phi),\\ x_{\mathrm{xxY}}(k,\theta,\phi) &= 2\,x(k,\theta,\phi-\Delta_\phi) - x(k,\theta,\phi-2\Delta_\phi), \end{aligned} \quad (11)$$

to the patterns Yxx and xxY, we produced respectively 170 and 186 extrapolated chips.

Next, we calculated the PCC for the same test sets described in Table 3. However, we used the subsets of data obtained through interpolation/extrapolation. The PCC obtained using those data as the basis for classification are listed in the last column of Table 4. In Fig. 24, the

graphs show the PCC achieved considering different data sources as the basis for classification: original EMC synthetic data, fake synthetic data, and interpolated/extrapolated EMC synthetic data. Each graph shows the results of the experiment according to each of the test sets detailed in Tables 3 and 4.

Observing these graphs and those of the MSE analysis (Section IV-D2), we verify that the results converge approximately around the same amount of training epochs, leading us to rely on the interval between 75 and 200 for application purposes. Regardless of the test set, we also verify that the PCC achieved with the fake synthetic data is always higher than that referring to the interpolated/extrapolated EMC synthetic data, which rules out the need for a hypothesis test. Therefore, as the basis for classification, the fake synthetic data leads to a significantly more accurate result than interpolated/extrapolated EMC synthetic data.

V. CONCLUSION

This paper proposed a method that uses a modified version of the pix2pix cGAN architecture to produce tailored synthetic data for noncooperative targets with specific elevation and azimuth angles. The methodology involves training the cGAN to interpolate and extrapolate SAR images based on input chips with different aspect angles. The convergence and collapsing analyses demonstrate the effectiveness of the proposed method in producing synthetic data that closely resemble real SAR images, indicating a successful adaptation of the cGAN approach to the SAR domain. Furthermore, the study uses a previously proposed model-based algorithm to evaluate the utility of the generated fake synthetic data for target classification. Experimental results show that the classification performance using fake synthetic data is remarkably close to that achieved using original EMC synthetic data, which serves as a benchmark. The article demonstrates that the fake synthetic data approach presents a viable alternative when EMC data is limited, and it outperforms simple interpolation/extrapolation techniques commonly employed. By employing cGANs to generate synthetic data, this paper paves the way for new avenues for enhancing target classification accuracy in SAR imagery, particularly in scenarios where acquiring real-world data is challenging. The findings presented in this paper shed light on the potential of synthetic data generation techniques to improve the performance of ATR algorithms, contributing to advancements in remote sensing.

REFERENCES

[1] A. Moreira, P. Prats-Iraola, M. Younis, G. Krieger, I. Hajnsek, and K. P. Papathanassiou, "A tutorial on synthetic aperture radar," *IEEE Geosci. Remote Sens. Mag.*, vol. 1, no. 1, pp. 6–43, Mar. 2013. [Online]. Available: https://ieeexplore.ieee.org/document/6504845, doi: 10.1109/MGRS.2013.2248301.

[2] I. G. Cumming and F. H. Wong, *Digital Processing of Synthetic Aperture Radar Data*, vol. 1. Norwood, MA, USA: Artech House, 2005.

[3] D. Blacknell and L. Vignaud, *Radar Automatic Target Recognition (ATR) and Non-Cooperative Target Recognition (NCTR)*. Edison, NJ, USA: IET, 2013.

[4] K. El-Darymli, E. W. Gill, P. Mcguire, D. Power, and C. Moloney, "Automatic target recognition in synthetic aperture radar imagery: A state-of-the-art review," *IEEE Access*, vol. 4, pp. 6014–6058, 2016. [Online]. Available: https://ieeexplore.ieee.org/document/7572958, doi: 10.1109/ACCESS.2016.2611492.

[5] T. D. Ross, S. W. Worrell, V. J. Velten, J. C. Mossing, and M. L. Bryant, "Standard SAR ATR evaluation experiments using the MSTAR public release data set," *Proc. SPIE*, vol. 3370, Sep. 1998, pp. 566–573, doi: 10.1117/12.321859.

[6] B. Lewis, T. Scarnati, E. Sudkamp, J. Nehrbass, S. Rosencrantz, and E. Zelnio, "A SAR dataset for ATR development: The synthetic and measured paired labeled experiment (SAMPLE)," *Proc. SPIE*, vol. 10987, May 2019, Art. no. 109870H, doi: 10.1117/12.2523460.

[7] G. F. Araujo, R. Machado, and M. I. Pettersson, "A tailored cGAN SAR synthetic data augmentation method for ATR application," in *Proc. IEEE Radar Conf. (RadarConf)*, San Antonio, TX, USA, May 2023, pp. 1–6, doi: 10.1109/RadarConf2351548.2023.10149587.

[8] F. Rosenblatt, "The perceptron: A probabilistic model for information storage and organization in the brain," *Psychol. Rev.*, vol. 65, no. 6, pp. 386–408, Nov. 1958, doi: 10.1037/h0042519.

[9] J. P. Mueller and L. Massaron, *Deep Learning for Dummies*. Hoboken, NJ, USA: Wiley, 2019.

[10] Y. L. Cun, B. Boser, J. S. Denker, R. E. Howard, W. Habbard, L. D. Jackel, and D. Henderson, *Handwritten Digit Recognition With a Back-Propagation Network*. San Francisco, CA, USA: Morgan Kaufmann, 1990, pp. 396–404.

[11] I. Goodfellow, Y. Bengio, and A. Courville, *Deep Learning*. Cambridge, MA, USA: MIT Press, 2016.

[12] L. Deng, "The MNIST database of handwritten digit images for machine learning research [best of the web]," *IEEE Signal Process. Mag.*, vol. 29, no. 6, pp. 141–142, Nov. 2012. [Online]. Available: https://ieeexplore.ieee.org/document/6296535, doi: 10.1109/MSP.2012.2211477.

[13] P. Isola, J.-Y. Zhu, T. Zhou, and A. A. Efros, "Image-to-image translation with conditional adversarial networks," in *Proc. IEEE Conf. Comput. Vis. Pattern Recognit. (CVPR)*, Honolulu, HI, USA, Jul. 2017, pp. 5967–5976, doi: 10.1109/CVPR.2017.632.

[14] J. Guo, B. Lei, C. Ding, and Y. Zhang, "Synthetic aperture radar image synthesis by using generative adversarial nets," *IEEE Geosci. Remote Sens. Lett.*, vol. 14, no. 7, pp. 1111–1115, Jul. 2017. [Online]. Available: https://ieeexplore.ieee.org/abstract/document/7927706, doi: 10.1109/LGRS.2017.2699196.

[15] B. Lewis, J. Liu, and A. Wong, "Generative adversarial networks for SAR image realism," *Proc. SPIE*, vol. 10647, Apr. 2018, Art. no. 1064709, doi: 10.1117/12.2301387.

[16] H. Huang, F. Zhang, Y. Zhou, Q. Yin, and W. Hu, "High resolution SAR image synthesis with hierarchical generative adversarial networks," in *Proc. IEEE Int. Geosci. Remote Sens. Symp. (IGARSS)*, Yokohama, Japan, Jul. 2019, pp. 2782–2785, doi: 10.1109/IGARSS.2019.8900494.

[17] J. Zhai, X. Dang, F. Chen, X. Xie, Y. Zhu, and H. Yin, "SAR image generation using structural Bayesian deep generative adversarial network," in *Proc. Photon. Electromagn. Res. Symp.-Fall (PIERS-Fall)*, Xiamen, China, Dec. 2019, pp. 1386–1392, doi: 10.1109/PIERS-Fall48861.2019.9021403.

[18] W. Zhang, Y. Zhu, and Q. Fu, "Semi-supervised deep transfer learning-based on adversarial feature learning for label limited SAR target recognition," *IEEE Access*, vol. 7, pp. 152412–152420, 2019, doi: 10.1109/ACCESS.2019.2948404.

[19] C. Zheng, X. Jiang, and X. Liu, "Semi-supervised SAR ATR via multi-discriminator generative adversarial network," *IEEE Sensors J.*, vol. 19, no. 17, pp. 7525–7533, Sep. 2019. [Online]. Available: https://ieeexplore.ieee.org/document/8707959, doi: 10.1109/JSEN.2019.2915379.

[20] Z. Luo, X. Jiang, and X. Liu, "Synthetic minority class data by generative adversarial network for imbalanced SAR target recognition," in *Proc. IEEE Int. Geosci. Remote Sens. Symp. (IGARSS)*, Waikoloa, HI, USA, Sep. 2020, pp. 2459–2462, doi: 10.1109/IGARSS39084.2020.9323439.

[21] Y. Guo, L. Du, D. Wei, and C. Li, "Robust SAR automatic target recognition via adversarial learning," *IEEE J. Sel. Topics Appl. Earth Observ. Remote Sens.*, vol. 14, pp. 716–729, Nov. 2021. [Online]. Available: https://ieeexplore.ieee.org/document/9264634, doi: 10.1109/JSTARS.2020.3039235.

[22] C. Mao, L. Huang, Y. Xiao, F. He, and Y. Liu, "Target recognition of SAR image based on CN-GAN and CNN in complex environment," *IEEE Access*, vol. 9, pp. 39608–39617, 2021. [Online]. Available: https://ieeexplore.ieee.org/document/9371694, doi: 10.1109/ACCESS.2021.3064362.

[23] D. Vint, M. Anderson, Y. Yang, C. Ilioudis, G. Di Caterina, and C. Clemente, "Automatic target recognition for low resolution foliage penetrating SAR images using CNNs and GANs," *Remote Sens.*, vol. 13, no. 4, p. 596, Feb. 2021. [Online]. Available: https://www.mdpi.com/2072-4292/13/4/596, doi: 10.3390/rs13040596.

[24] X. Hu, W. Feng, Y. Guo, and Q. Wang, "Feature learning for SAR target recognition with unknown classes by using CVAE-GAN," *Remote Sens.*, vol. 13, no. 18, p. 3554, Sep. 2021. [Online]. Available: https://www.mdpi.com/2072-4292/13/18/3554, doi: 10.3390/rs13183554.

[25] J. Oh and M. Kim, "PeaceGAN: A GAN-based multi-task learning method for SAR target image generation with a pose estimator and an auxiliary classifier," *Remote Sens.*, vol. 13, no. 19, p. 3939, Oct. 2021. [Online]. Available: https://www.mdpi.com/2072-4292/13/19/3939, doi: 10.3390/rs13193939.

[26] C. Du and L. Zhang, "Adversarial attack for SAR target recognition based on UNet-generative adversarial network," *Remote Sens.*, vol. 13, no. 21, p. 4358, Oct. 2021. [Online]. Available: https://www.mdpi.com/2072-4292/13/21/4358, doi: 10.3390/rs13214358.

[27] S. Du, J. Hong, Y. Wang, and Y. Qi, "A high-quality multicategory SAR images generation method with multiconstraint GAN for ATR," *IEEE Geosci. Remote Sens. Lett.*, vol. 19, pp. 1–5, 2022, doi: 10.1109/LGRS.2021.3065682.

[28] X. Ma, K. Ji, L. Zhang, S. Feng, B. Xiong, and G. Kuang, "An open set recognition method for SAR targets based on multitask learning," *IEEE Geosci. Remote Sens. Lett.*, vol. 19, pp. 1–5, 2022, doi: 10.1109/LGRS.2021.3079418.

[29] S. Du, J. Hong, Y. Wang, K. Xing, and T. Qiu, "Physical-related feature extraction from simulated SAR image based on the adversarial encoding network for data augmentation," *IEEE Geosci. Remote Sens. Lett.*, vol. 19, pp. 1–5, 2022. [Online]. Available: https://ieeexplore.ieee.org/document/9510178, doi: 10.1109/LGRS.2021.3100642.

[30] C. Grohnfeldt, M. Schmitt, and X. Zhu, "A conditional generative adversarial network to fuse SAR and multispectral optical data for cloud removal from Sentinel-2 images," in *Proc. IEEE Int. Geosci. Remote Sens. Symp. (IGARSS)*, Valencia, Spain, Jul. 2018, pp. 1726–1729, doi: 10.1109/IGARSS.2018.8519215.

[31] W. He and N. Yokoya, "Multi-temporal Sentinel-1 and -2 data fusion for optical image simulation," *ISPRS Int. J. Geo-Inf.*, vol. 7, no. 10, p. 389, Sep. 2018, doi: 10.3390/ijgi7100389.

[32] K. Bittner, P. d'Angelo, M. Körner, and P. Reinartz, "DSM-to-LoD2: Spaceborne stereo digital surface model refinement," *Remote Sens.*, vol. 10, no. 12, p. 1926, Nov. 2018, doi: 10.3390/rs10121926.

[33] X. Niu, M. Gong, T. Zhan, and Y. Yang, "A conditional adversarial network for change detection in heterogeneous images," *IEEE Geosci. Remote Sens. Lett.*, vol. 16, no. 1, pp. 45–49, Jan. 2019. [Online]. Available: https://ieeexplore.ieee.org/document/8471225, doi: 10.1109/LGRS.2018.2868704.

[34] G. Li, Z. Sun, and Y. Zhang, "ISAR target recognition using pix2pix network derived from cGAN," in *Proc. Int. Radar Conf.*, Toulon, France, 2019, pp. 397–400. [Online]. Available: https://ieeexplore.ieee.org/abstract/document/9078939, doi: 10.1109/RADAR41533.2019.171345.

[35] A. Patel, M. Patel, T. Gadhiya, and A. K. Roy, "PolSAR band-to-band image translation using conditional adversarial networks," in *Proc. IEEE SENSORS*, Montreal, QC, Canada, 2019, pp. 1–4. [Online]. Available: https://ieeexplore.ieee.org/document/8956702, doi: 10.1109/SENSORS43011.2019.8956702.

[36] F. Ma, F. Gao, J. Sun, H. Zhou, and A. Hussain, "Weakly supervised segmentation of SAR imagery using superpixel and hierarchically adversarial CRF," *Remote Sens.*, vol. 11, no. 5, p. 512, Mar. 2019. [Online]. Available: https://www.mdpi.com/2072-4292/11/5/512, doi: 10.3390/rs11050512.

[37] J. D. Bermudez, P. N. Happ, R. Q. Feitosa, and D. A. B. Oliveira, "Synthesis of multispectral optical images from SAR/optical multitemporal data using conditional generative adversarial networks," *IEEE Geosci. Remote Sens. Lett.*, vol. 16, no. 8, pp. 1220–1224, Aug. 2019. [Online]. Available: https://ieeexplore.ieee.org/document/8637007, doi: 10.1109/LGRS.2019.2894734.

[38] H. Daquan, J. Tian, S. Yongkun, and W. Chen, "A CGAN-based FOPEN target detection method for bi-frequency SAR," in *Proc. Int. Conf. Image, Video Process. Artif. Intell.* Shanghai, China: SPIE, 2020, pp. 101–106, doi: 10.1117/12.2579696.

[39] Y. Li, R. Fu, X. Meng, W. Jin, and F. Shao, "A SAR-to-optical image translation method based on conditional generation adversarial network (cGAN)," *IEEE Access*, vol. 8, pp. 60338–60343, 2020, doi: 10.1109/ACCESS.2020.2977103.

[40] L. Maggiolo, D. Solarna, G. Moser, and S. B. Serpico, "Automatic area-based registration of optical and SAR images through generative adversarial networks and a correlation-type metric," in *Proc. IEEE Int. Geosci. Remote Sens. Symp. (IGARSS)*, Waikoloa, HI, USA, Sep. 2020, pp. 2089–2092, doi: 10.1109/IGARSS39084.2020.9323235.

[41] S. Björk, S. N. Anfinsen, E. Næsset, T. Gobakken, and E. Zahabu, "Generation of LiDAR-predicted forest biomass maps from radar backscatter with conditional generative adversarial networks," in *Proc. IEEE Int. Geosci. Remote Sens. Symp. (IGARSS)*, Waikoloa, HI, USA, Sep. 2020, pp. 4327–4330, doi: 10.1109/IGARSS39084.2020.9324296.

[42] B. Huang, Z. Li, C. Yang, F. Sun, and Y. Song, "Single satellite optical imagery dehazing using SAR image prior based on conditional generative adversarial networks," in *Proc. IEEE Winter Conf. Appl. Comput. Vis. (WACV)*, Snowmass, CO, USA, Mar. 2020, pp. 1795–1802, doi: 10.1109/WACV45572.2020.9093471.

[43] S. Wang, J. Guo, Y. Zhang, Y. Hu, C. Ding, and Y. Wu, "TomoSAR 3D reconstruction for buildings using very few tracks of observation: A conditional generative adversarial network approach," *Remote Sens.*, vol. 13, no. 24, p. 5055, Dec. 2021. [Online]. Available: https://www.mdpi.com/2072-4292/13/24/5055, doi: 10.3390/rs13245055.

[44] J. N. Turnes, J. D. B. Castro, D. L. Torres, P. J. S. Vega, R. Q. Feitosa, and P. N. Happ, "Atrous cGAN for SAR to optical image translation," *IEEE Geosci. Remote Sens. Lett.*, vol. 19, pp. 1–5, 2022. [Online]. Available: https://ieeexplore.ieee.org/document/9241239, doi: 10.1109/LGRS.2020.3031199.

[45] L. E. Christovam, M. H. Shimabukuro, M. D. L. B. T. Galo, and E. Honkavaara, "Pix2pix conditional generative adversarial network with MLP loss function for cloud removal in a cropland time series," *Remote Sens.*, vol. 14, no. 1, p. 144, Dec. 2021. [Online]. Available: https://www.mdpi.com/2072-4292/14/1/144, doi: 10.3390/rs14010144.

[46] X. Yang, J. Zhao, Z. Wei, N. Wang, and X. Gao, "SAR-to-optical image translation based on improved CGAN," *Pattern Recognit.*, vol. 121, Jan. 2022, Art. no. 108208. [Online]. Available: https://www.sciencedirect.com/science/article/pii/S0031320321003897, doi: 10.1016/j.patcog.2021.108208.

[47] C. Wang, J. Pei, X. Liu, Y. Huang, D. Mao, Y. Zhang, and J. Yang, "SAR target image generation method using azimuth-controllable generative adversarial network," *IEEE J. Sel. Topics Appl. Earth Observ. Remote Sens.*, vol. 15, pp. 9381–9397, Oct. 2022, doi: 10.1109/JSTARS.2022.3218369.

[48] A. Radford, L. Metz, and S. Chintala, "Unsupervised representation learning with deep convolutional generative adversarial networks," 2015, *arXiv:1511.06434*, doi: 10.48550/arXiv.1511.06434.

[49] O. Ronneberger, P. Fischer, and T. Brox, "U-Net: Convolutional networks for biomedical image segmentation," in *Medical Image Computing and Computer-Assisted Intervention*. Munich, Germany: Springer, 2015, pp. 234–241, doi: 10.1007/978-3-319-24574-4_28.

[50] G. F. Araujo, R. Machado, and M. I. Pettersson, "Non-cooperative SAR automatic target recognition based on scattering centers models," *Sensors*, vol. 22, no. 3, p. 1293, Feb. 2022, doi: 10.3390/s22031293.

GUSTAVO F. ARAUJO received the B.S.E.E. degree from the Federal University of Juiz de Fora (UFJF), Minas Gerais, Brazil, the Specialization degree in geoprocessing from the University of Brasilia (UNB), Brazil, in 2013, and the M.Sc. degree in electronic engineering from the Aeronautics Institute of Technology (ITA), São José dos Campos, São Paulo, Brazil, in 2016, where he is currently pursuing the Ph.D. degree.

Since 1996, he has been with the Brazilian Air Force as an Engineer Officer, performing the following functions, such as the Head of the Operation and Maintenance of Communications, Telemetry, and Radar Systems with the Alcântara Space Center, Alcântara, Brazil;

the Head of the Maintenance for Electronic Systems of the E-99 (AEW&C) and R-99 (Remote Sensing) Aircraft with Anápolis Air Force Base, Anápolis, Brazil; the Head of the Maintenance for Electronic Systems of the Maritime Patrol Aircraft (P-3AM) with Salvador Air Force Base, Salvador, Brazil; and an Operational Research Officer with the Air Command, and Command and Control Officer of the Air Force Chief Staff, Brasília, Brazil. His research is related to remote sensing. His main research interests include SAR automatic target recognition (ATR), computer vision, image processing, radar signal processing, digital signal processing, and artificial intelligence.

RENATO MACHADO (Senior Member, IEEE) received the B.S.E.E. degree from São Paulo State University (UNESP), Ilha Solteira, Brazil, in 2001, and the M.Sc. and Ph.D. degrees in electrical engineering from the Federal University of Santa Catarina (UFSC), Florianópolis, Brazil, in 2004 and 2008, respectively. From August 2006 to June 2007, he was a Visiting Ph.D. Scholar with the Department of Electrical Engineering, Arizona State University, Tempe, AZ, USA. From 2007 to 2008, he was with the Research and Development Department, Nokia Institute of Technology, Brasília. From August 2009 to December 2017, he was an Assistant Professor (2008–2016) and an Associate Professor (2017) with the Federal University of Santa Maria, Brazil, where he lectured many courses in bachelor's and graduate programs. From November 2013 to February 2015, he was a Visiting Research Fellow with the Blekinge Institute of Technology (BTH) in partnership with Saab AB. He assumed different positions in the institution, such as the Research Leader of the Communications and Signal Processing Research Group, a Coordinator of the Telecommunications Engineering Program, and the Director of the Aerospace Science Laboratory. Since December 2017, he has been an Associate Professor with the Aeronautics Institute of Technology (ITA), where he is currently a Research Leader of the Digital and Signal Processing Laboratory and SAR and the Radar Signal Processing Laboratory. His research interests include SAR processing, SR image processing, change detection, radar signal processing, digital signal processing, and artificial intelligence signal processing. He is a member of the Brazilian Telecommunication Society.

MATS I. PETTERSSON (Senior Member, IEEE) received the M.Sc. degree in engineering physics, the Licentiate degree in radio and space science, and the Ph.D. degree in signal processing from the Chalmers University of Technology, Gothenburg, Sweden, in 1993, 1995, and 2000, respectively. He was with Mobile Communication Research at Ericsson, Lund, Sweden. He was also with the Swedish Defense Research Agency (FOI), for ten years. At FOI, he focused on ultrawideband low-frequency SAR systems. Since 2005, he has been with the Blekinge Institute of Technology (BTH), Karlskrona, Sweden, where he is currently a Full Professor. He has authored or coauthored more than 250 scientific publications, of which more than 70 are in peer-reviewed scientific journals. His research is related to radar surveillance and remote sensing. His main research interests include SAR processing, space-time adaptive processing (STAP), high-resolution SAR change detection, automotive radar, radio occultation, THz SAR, and computer vision.